45th AIAA Aerospace Sciences Meeting and Exhibit
8 - 11 January 2007, Reno, Nevada

AIAA 2007-1455

Large-Eddy Simulation of Breaking Waves Using Embedded-Boundary/Level-Set Method

Jianming Yang* and Frederick Stern†

IIHR - Hydroscience & Engineering, University of Iowa, Iowa City, IA 52242-1585, USA

In this paper, we present a sharp interface method for the large-eddy simulation of breaking waves generated by immersed bodies. Our method is based on the level set formulation for two-phase incompressible flows, in which the interface between two immiscible fluids, e.g., air and water, is represented by the zero level set. The density jump and pressure jump due to surface tension are treated in a sharp interface manner using a boundary condition capturing method (ghost fluid method). The immersed bodies are treated using a sharp interface direct forcing immersed boundary method. A Lagrangian dynamic Smagorinsky subgrid-scale model is adopted for the large-eddy simulations of turbulent two-phase flows. The numerical method is validated using several examples, such as 2D solitary wave propagation, 2D dam-break problem, and 3D rising bubble. And the large-eddy simulations of breaking waves generated by a submerged hydrofoil and a surface-mounted bump are described in detail.

I. Introduction

Wave breaking is an important subject of studies in geophysics and ocean, coastal and marine engineering. Two very common breaking waves are spilling and plunging breakers. The former usually presents a foam separation region riding on the forward face of the wave; while the latter features the overturning of the front face of the wave, large splash near the wave base, and significant air entrainment and bubble formation. Although considerable progress in theoretical, experimental, and numerical aspects has been made during the past decades, several substantial characteristics of breakers in nature have not been investigated in detail. Among them are air entrainment, instabilities and vortex structures, and turbulence especially for 3D flows and complex geometries, which present more challenges to further computational studies, due to demanding modeling and numerical methods and humongous computer power requirement.

In numerical simulations, to take air entrainment into account, single-phase models that only consider the free surface water flows are no longer applicable and two-phase models that solve both air and water flows have to be adopted. Furthermore, to understand the instantaneous role of turbulence in the wave breaking process, three-dimensional models have to be used as the vortex stretching in the third dimension is missing and the turbulence becomes unrealistic in two-dimensional models. Recent years, the Reynolds-averaged Navier-Stokes (RANS) equations based calculations of free-surface turbulent flows have become common practice in naval hydrodynamics and ocean/coastal engineering fields.[5,37] However, RANS models are usually too dissipative for the simulations of highly unsteady breaking waves. On the other hand, in the large-eddy simulation (LES) of turbulence, only the subgrid scales are modeled and the large, energy-carrying scales are resolved. Thus, LES provides much more detailed information of turbulence than RANS, although with much higher computational cost due to the spatial and temporal resolution requirement.

As the computer power increases, the large-eddy simulations of many complicated turbulent flows become affordable and some results on LES of breaking waves have been reported in the literature recently. Although the calculations using LES methodologies in 2D computational space can provide some information beyond steady RANS models, as mentioned above, the instantaneous turbulence structures are unrealistic in a two-dimensional framework. In some three-dimensional large-eddy simulations of breaking waves,[10,36,11] single phase models were used and the air entrainment effects were ignored. In Ref. 26, a two-phase model was

*Post-doctoral Associate, AIAA Member.
†Professor of Mechanical Engineering.

adopted, thus the air entrainment was simulated. However, all the above work used relatively simple SGS models involving constant parameters relying on problem-dependent adjustments. Also, the fixed Eulerian Cartesian/curvilinear structured grids utilized in those papers limited their methods to simple geometries.

Currently, we are developing a high-fidelity and cost-effective computational tool for the simulations of three-dimensional two-phase (air/water) turbulent flows involving complex stationary/moving solid boundaries and strong air/water interactions such as breaking waves. In this paper, we shall concentrate on the LES of 3D breaking waves generated by a fully submerged NACA 0012 hydrofoil[12] and by a surface-mounted bump (profile given in Ref. 16). The particular interests are in the detailed wave breaking process, interactions of shed vortices and free surface waves, two-phase flow and turbulence, including three dimensional effects.

Our method is based on the level set formulation for two-phase incompressible flows in which the interface between two immiscible fluids, e.g., air and water, is represented by the zero level set. The density jump and pressure jump due to surface tension are treated in a sharp interface manner using a boundary condition capturing method (ghost fluid method). The immersed bodies are treated using a sharp interface direct forcing immersed boundary method . A Lagrangian dynamic Smagorinsky subgrid-scale model is adopted for the large-eddy simulations of turbulent two-phase flows. In Sec. II the mathematical model is described. Sec. III gives the numerical method. Then in Sec. IV the numerical method is validated using several examples, such as 2D solitary wave propagation, 2D dam-break problem, and 3D rising bubble. And the LES of breaking waves generated by a submerged hydrofoil and a surface-mounted bump are described in detail. Finally some conclusions are presented in Sec. V.

II. Mathematical Model

The level set formulation for the incompressible flows of two immiscible fluids separated by an interface given in Ref. 7 is used here. In this approach, one set of equations for both fluids are solved with the density and viscosity jumps across the interface linked by a Heaviside function.

II.A. Navier-Stokes Equations

The incompressible viscous flows of two immiscible fluids, e.g., air and water, are governed by the Navier-Stokes equations:

$$\frac{\partial \mathbf{u}}{\partial t} + \mathbf{u} \cdot \nabla \mathbf{u} = \frac{1}{\rho} \nabla \cdot (-p\mathbf{I} + \mathbf{T}) + \mathbf{g}, \tag{1}$$

$$\nabla \cdot \mathbf{u} = 0, \tag{2}$$

where t is the time, $\mathbf{u}$ is the velocity vector, p is the pressure, $\mathbf{I}$ is the unit tensor, ρ is the density, $\mathbf{g}$ represents the gravity force, and $\mathbf{T}$ is the viscous stress tensor defined as

$$\mathbf{T} = 2\mu\mathbf{S} = 2\mu \left[\frac{1}{2} \left(\nabla \mathbf{u} + (\nabla \mathbf{u})^T \right) \right] = \mu \left(\nabla \mathbf{u} + (\nabla \mathbf{u})^T \right), \tag{3}$$

with μ the dynamic viscosity, $\mathbf{S}$ the strain rate tensor and T the transpose operator.

Since the fluid properties are discontinuous across the interface, which is a function of time and space, density and viscosity are also functions of time and space and only known with given interface position. Their definitions will be deferred to Sec. II.D after the introduction of interface representation using level set.

II.B. Interface Jump Conditions

The velocity across the interface Γ is continuous, as the fluids are viscous and no phase change is considered here:

$$[\mathbf{u}] = 0, \tag{4}$$

and the jump condition for stress is

$$\left[\mathbf{n} \cdot \left(-p\mathbf{I} + \mu \left(\nabla \mathbf{u} + (\nabla \mathbf{u})^T \right) \right) \cdot \mathbf{n} \right] = \sigma\kappa, \tag{5}$$

where $[\ \cdot\ ]$ indicates the jump at the interface, i.e., $f_L^I - f_G^I$ for a variable f with superscript I denotes interface, $\mathbf{n}$ is the unit vector normal to the interface, σ is the coefficient of surface tension, and κ is the local curvature of the interface.

II.C. Interface Representation

Define the interface Γ as the zero level set of a signed distance function, ϕ, or the level set function, the position of the interface can be tracked by solving the level set evolution equation

$$\frac{\partial \phi}{\partial t} + \mathbf{u} \cdot \nabla \phi = 0. \tag{6}$$

To keep ϕ as a signed distance function in the course of evolution, we iterate the reinitialization equation for the level set function:[33]

$$\frac{\partial \phi}{\partial \tau} + S(\phi_o)\left(|\nabla \phi| - 1\right) = 0, \tag{7}$$

where τ is the pseudo time and $S(\phi_o)$ is the numerically smeared-out sign function

$$S(\phi_o) = \frac{\phi_o}{\sqrt{\phi_o^2 + h^2}}, \tag{8}$$

with ϕ_o the initial values of ϕ and h a small amount, usually the grid cell size, to smear out the sign function.

Since the level set function is a signed distance function, the interface normal and mean curvature can be readily calculated by applying standard finite difference to the level set function:

$$\mathbf{N} = \frac{\nabla \phi}{|\nabla \phi|}, \tag{9}$$

and

$$\kappa = \nabla \cdot \mathbf{N} = \nabla \cdot \frac{\nabla \phi}{|\nabla \phi|}, \tag{10}$$

respectively.

II.D. Fluid Properties

With the level set function defined, the fluid properties, such as density and viscosity, are given by the following equations:

$$\begin{aligned} \rho &= \rho_G + (\rho_L - \rho_G) H(\phi), \\ \mu &= \mu_G + (\mu_L - \mu_G) H(\phi), \end{aligned} \tag{11}$$

where the subscripts G and L represent gas and liquid phase, respectively, and the Heaviside function is defined as

$$H(\phi) = \begin{cases} 1 & \text{if} \quad \phi \geq 0 \\ 0 & \text{if} \quad \phi < 0 \end{cases} \tag{12}$$

In this paper, the viscosity is smoothed over a transition region across the interface as

$$\mu = \mu_G + (\mu_L - \mu_G) H_\varepsilon(\phi), \tag{13}$$

using the smoothed Heaviside function[33]

$$H_\varepsilon(\phi) = \begin{cases} 1 & \text{if} \quad \phi > \varepsilon \\ \frac{1}{2}\left[1 + \frac{\phi}{\varepsilon} + \frac{1}{\pi}\sin\left(\frac{\pi\phi}{\varepsilon}\right)\right] & \text{if} \quad |\phi| \leq \varepsilon \\ 0 & \text{if} \quad \phi < -\varepsilon \end{cases} \tag{14}$$

Notice with a continuous viscosity and velocity field, the stress jump conditions Eq. (5) reduce to

$$[p] = p_L^I - p_G^I = -\sigma\kappa. \tag{15}$$

II.E. Subgrid-scale Model

In the LES approach, the Navier-Stokes equations are spatially filtered such that the large, energy carrying eddies are resolved and the small scale, dissipative eddies are modeled by a sub-grid scale stress model. After applied the filter operation to Eq. (1,2), we have

$$\frac{\partial \bar{\mathbf{u}}}{\partial t} + \bar{\mathbf{u}} \cdot \nabla \bar{\mathbf{u}} = -\frac{1}{\rho}\nabla \bar{p} - \nabla \cdot \bar{\tau} + \frac{1}{\rho}\nabla \cdot \left[\mu\left(\nabla \bar{\mathbf{u}} + (\nabla \bar{\mathbf{u}})^T\right)\right] + \mathbf{g}, \tag{16}$$

$$\nabla \cdot \bar{\mathbf{u}} = 0, \tag{17}$$

where $\bar{f}$ denotes the filter operation on a variable f, $\bar{\tau} = \overline{\mathbf{u}\mathbf{u}} - \bar{\mathbf{u}}\bar{\mathbf{u}}$ is the subgrid-scale (SGS) stress tensor, whose deviatoric part is parametrized by following the Smagorinsky procedure as:

$$\bar{\tau} - \frac{1}{3}\text{trace}(\bar{\tau})\mathbf{I} = -2\nu_t \bar{\mathbf{S}}. \tag{18}$$

And the turbulent eddy viscosity is defined as

$$\nu_t = C\Delta^2 |\bar{\mathbf{S}}|, \quad \text{and} \quad |\bar{\mathbf{S}}| = \sqrt{2\bar{\mathbf{S}} \cdot \bar{\mathbf{S}}}. \tag{19}$$

The model parameter C in the eddy viscosity definition has to be given to close the equations. In this paper the Lagrangian dynamic SGS model[29] is chosen as it can handle complex geometries without the requirement of homogeneous direction(s). Therefore, Eq. (16) can be rewritten as the following form

$$\frac{\partial \bar{\mathbf{u}}}{\partial t} + \bar{\mathbf{u}} \cdot \nabla \bar{\mathbf{u}} = -\frac{1}{\rho}\nabla \bar{p} + \nabla \cdot \left[\nu_t\left(\nabla \bar{\mathbf{u}} + (\nabla \bar{\mathbf{u}})^T\right)\right] + \frac{1}{\rho}\nabla \cdot \left[\mu\left(\nabla \bar{\mathbf{u}} + (\nabla \bar{\mathbf{u}})^T\right)\right] + \mathbf{g}, \tag{20}$$

with the trace of subgrid-scale stress tensor $\frac{1}{3}\text{trace}(\bar{\tau})$ incorporated into $\bar{p}$. Also, we cannot have an effective total viscosity by $\mu + \rho\nu_t$ since ρ is discontinuous across the interface in the present sharp interface treatment.

III. Numerical Method

III.A. Navier-Stokes Solver

The finite difference method is used to discretize the Navier-Stokes equations on a non-uniform staggered Cartesian grid, in which the velocity components u, v, and w are defined at centers of cell faces in the x, y, and z directions, respectively, and all other variables, i.e., p, ϕ, ρ, μ, and ν_t are defined at cell centers. A semi-implicit time-advancement scheme is adopted to integrate the momentum equations with the second-order Crank-Nicolson scheme for the diagonal viscous terms and the second-order Adams-Bashforth scheme for the convective terms and other viscous terms. A four-step fractional-step method[9] is employed for velocity-pressure coupling, in which a pressure Poisson equation is solved to enforce the continuity equation:

- Predictor:
$$\frac{\hat{u}_i - u_i^n}{\Delta t} = \frac{1}{2}\left[3A_i^n - A_i^{n-1}\right] + \frac{1}{2}\left[C_i^{n+1} + C_i^n\right] - \text{Grad}_i(p^n) + g_i, \tag{21}$$

- First Corrector:
$$\frac{u_i^* - \hat{u}_i}{\Delta t} = \text{Grad}_i(p^n) \tag{22}$$

- Pressure Poisson Equation:
$$\frac{\partial}{\partial x_i}\text{Grad}_i(p^{n+1}) = \frac{1}{\Delta t}\frac{\partial u_i^*}{\partial x_i} \tag{23}$$

- Second Corrector:
$$\frac{u_i^{n+1} - u_i^*}{\Delta t} = -\text{Grad}_i(p^{n+1}) \tag{24}$$

where superscript n denotes time step, subscript $i = 1, 2, 3$ represents i-coordinate, A and C denote terms treated by the Adams-Bashforth and Crank-Nicolson schemes, $\hat{u}$ and u^* are the first and second intermediate velocities, respectively. $\text{Grad}_i(p)$ is a pressure gradient term defined at the center of cell face (collocated with velocity components) with the jump conditions incorporated in (for similar definition, see Ref. 34). For example, in the x direction, we have

$$\text{Grad}(p)_{i+1/2} = \frac{1}{\rho_{i+1/2}} \frac{(p_{i+1} - p_i) + \sigma\kappa^I (H_{i+1} - H_i)}{\Delta x} \tag{25}$$

where H is the Heaviside function, the superscript I denotes interface. The cell face density is defined as

$$\rho_{i+1/2} = \rho_L \theta_{i+1/2} + \rho_G \left(1 - \theta_{i+1/2}\right), \tag{26}$$

with

$$\theta_{i+1/2} = \begin{cases} 1 & \phi_i \geq 0 \quad \text{and} \quad \phi_{i+1} \geq 0 \\ 0 & \phi_i < 0 \quad \text{and} \quad \phi_{i+1} < 0 \\ \frac{\phi_i}{|\phi_i| + |\phi_{i+1}|} & \phi_i \geq 0 \quad \text{and} \quad \phi_{i+1} < 0 \\ \frac{\phi_{i+1}}{|\phi_i| + |\phi_{i+1}|} & \phi_i < 0 \quad \text{and} \quad \phi_{i+1} \geq 0 \end{cases} \tag{27}$$

Note that the surface tension as a singular force doesn't appear in the momentum equations explicitly since it enters the system through the pressure jump condition. Also, Eq. (23) is rearranged to move the pressure jump condition into the right hand side.[25]

The above four-step time advancement scheme doesn't require special treatment of boundary conditions for the intermediate velocity to obtain an overall second order splitting. The pressure correction methods are not applicable here because the density and pressure are treatment in a sharp interface manner and the following equality cannot be applied directly

$$\frac{1}{\rho}\nabla p^{n+1} = \frac{1}{\rho}\nabla p^n + \frac{1}{\rho}\nabla\psi, \tag{28}$$

with ψ for the pressure correction or increment.

In Eq. (21) the convective terms are discretized using a third-order QUICK scheme[23] and higher-order WENO schemes[18] are available. All other terms are discretized with the standard second-order central difference scheme. And Eq. (21) is approximated with the approximate factorization method[4] and the resulting tridiagonal linear equations are solved with the parallel tridiagonal system solver given in Ref. 28. The parallelization is done via a domain decomposition technique using the MPI library. The pressure Poisson equation is solved using a multigrid-preconditioned Krylov subspace solver from the PETSc library.[3] In general, this is the most expensive part of the whole algorithm.

III.B. Level Set Solver

The level set equation and the reinitialization equation are solved using the third-order TVD Runge-Kutta scheme[32] for time advancement and the fifth-order Hamilton-Jacobi Weighted-ENO (HJ-WENO) scheme[17] for spatial discretization. The additional solve of these equations does not pose a significant overhead as they are solved in a narrow band about several grid-cell wide as detailed in Ref. 30.

III.C. Immersed Boundary Treatment

The embedded boundary formulation in Ref. 38 is adopted here to treat the immersed boundaries/bodies in a non-uniform Cartesian grid. In this approach, the grid generation for complex geometries is trivial as the requirement that the grid points coincide with the boundary, which is imperative for body-fitted methods, is relaxed; while the solution near the immersed boundary is reconstructed using momentum forcing in a sharp-interface manner. The detailed procedure is given in Ref. 1, 38 and summarized here.

The first step is to establish the grid-interface relation with a given immersed boundary description, such as parametrized curve/surface or triangulation. In this step all Cartesian grid nodes are split into the three categories shown in Fig. 1: (1): *fluid-points*, which are points in the fluid phase; (2) *forcing points*, which are grid points in the fluid phase with one or more neighboring points in the solid phase; (3) *solid-points*,

which are points in the solid phase. The Navier-Stokes solver described in the previous section is applied on all points of the Eulerian grid as if the fluid/solid interface is not present. The effect of immersed boundary on the flow is introduced through the discrete forcing function, f_i. It is computed only at the forcing points by substituting $\hat{u}_i^n$ with u_f in Eq. (21) and solving for f_i:

$$f_i^n = \frac{u_f - u_i^{n-1}}{\Delta t} - \mathrm{RHS}_i^n, \tag{29}$$

where RHS_i^n denotes the right-hand-side of Eq. (21). In the special case where the interface and the forcing point coincide, u_f is simply the local velocity on the rigid body, and therefore the boundary condition one wishes to enforce. In the general case, however, the points on the Eulerian grid and the interface almost never coincide and u_f has to be computed using some interpolation strategy. An example is shown in Fig. 1, where the velocity at the forcing point is computed by means of linear interpolation that involves the projection of the forcing point on the interface (point 1 in Fig 1) and two points in the fluid phase (points 2 and 3 in Fig 1). For the semi-implicit time advancement scheme used here, a provisional step is applied with all terms by the Crank-Nicolson scheme treated using the forward Euler scheme. Then the forcing function in Eq. (29) can be evaluated straightforward.[20,2] The above procedure has been extensively tested for a variety of laminar and turbulent flow problems involving stationary and moving immersed boundaries with results in excellent agreement with reference computations and experiments.[1,2,38]

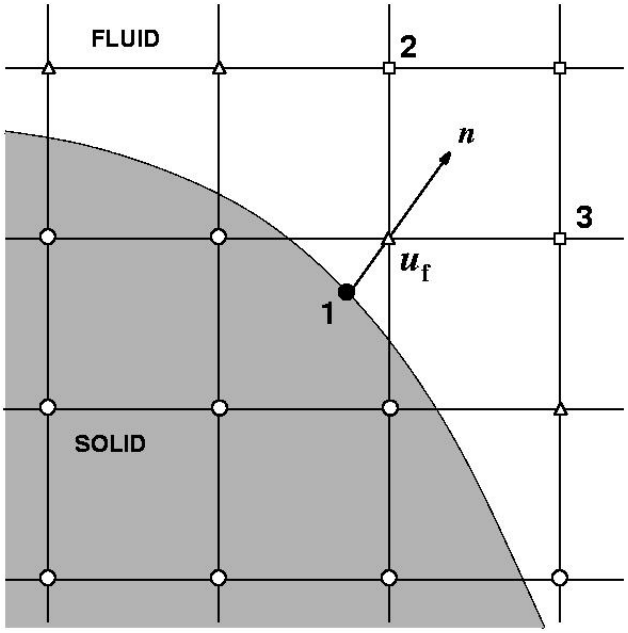

Figure 1. Grid/interface relation and Interpolation stencil for u_f (point 1, 2, and 3): ○ *solid points*; □ *fluid points*; △ *forcing points*.

III.D. Time Step Restriction

The time step Δt is restricted by the CFL condition, gravity, and surface tension. Follow Ref. 19 and choose a CFL restriction of 0.5, we have

$$\Delta t \leq 0.5 \left(\frac{C_{cfl} + \sqrt{(C_{cfl})^2 + 4\,(G_{cfl})^2 + 4\,(S_{cfl})^2}}{2} \right)^{-1}, \tag{30}$$

with the convective time step restriction

$$C_{cfl} = \max\left(\frac{|u|}{\Delta x} + \frac{|v|}{\Delta y} + \frac{|w|}{\Delta z} \right), \tag{31}$$

the time step restriction due to gravity

$$G_{cfl} = \sqrt{\frac{|g_x|}{\Delta x} + \frac{|g_y|}{\Delta y} + \frac{|g_z|}{\Delta z}}, \tag{32}$$

and the time step restriction due to surface tension

$$S_{cfl} = \sqrt{\frac{\sigma|\kappa|}{\rho_G \left(\min(\Delta x, \Delta y, \Delta z)\right)^2}}. \tag{33}$$

IV. Results

IV.A. Validation Cases

In this section, the basic solver for unsteady incompressible two-phase flows is validated against several widely-used test cases: the propagation of a solitary wave and its run-up on a vertical wall, a 2D dam-break problem, and a 3D rising spherical cap bubble in a quiescent liquid.

IV.A.1. Run-up of a Solitary Wave

Solitary waves have been extensively studied. A solitary wave has a symmetrical profile with one crest; it can propagate with a constant speed and maintain its original shape. Here we choose the case presented in Ref. 6 to validate our numerical method. This case has also been used by many researchers, such as Ref. 39, 24 among others. Here we use the computational setup as shown in Fig. 2. The size of the enclosed channel is $20H \times 2H$ with H the still water depth. Instead of specifying an initial wave profile, velocity and pressure field by Laitone's[22] approximate solution,[6] we initialize the interface as a still Boussinesq profile[31] in hydrostatic balance for a reflected solitary wave at its peak height A_0 at the left vertical wall:

$$A(x,0) = A_0/\cosh^2\left(\frac{\sqrt{3A_0}}{2}x\right). \tag{34}$$

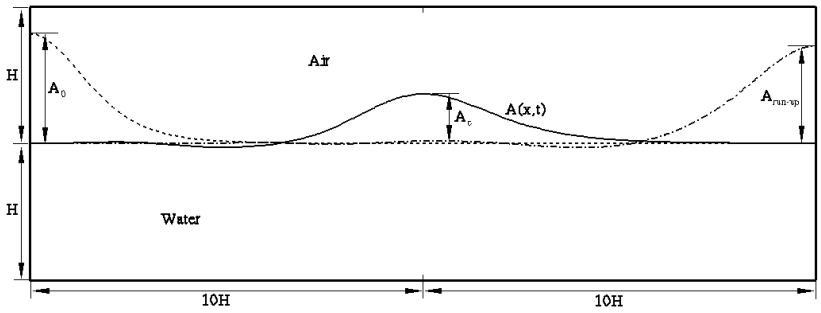

Figure 2. Sketch of computational setup for a traveling solitary wave in an enclosed channel.

As a result of gravity g a wave will be generated and can be considered as a solitary wave when the effects of the left wall become very small. This solitary wave propagates to the right side and hits the right wall. The amplitude of the solitary wave when it passes the middle of the channel is chosen as the reference A_c. The height it climbs to is called run-up A_{run-up}.

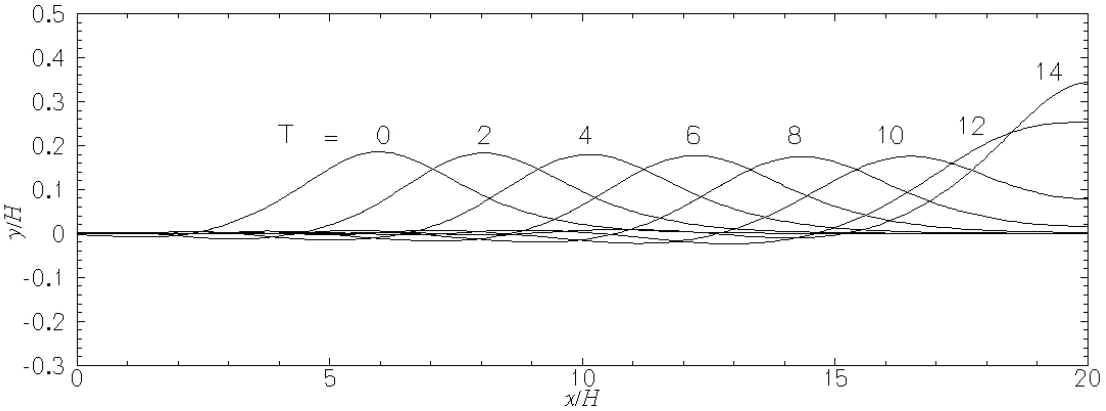

Figure 3. Traveling trains and run-up of a solitary wave at different times.

In all cases of different A_0 considered, the density and viscosity ratio are $\rho_{air}/\rho_{water} = 1.2 \times 10^{-3}$ and $\mu_{air}/\mu_{water} = 1.8 \times 10^{-2}$, respectively. The Reynolds number is $Re = \rho_{water} c_{wave} H/\mu_{water} = 5 \times 10^4$ with c_{wave} the theoretical solitary wave speed $c_{wave} = \sqrt{gH} = 1$. A grid of size 200×100, uniform in both the x and y directions, is used for all the computations. The resolution in the y direction is much higher than that in the x direction as the flow has a large gradient in the vertical direction. The half thickness of the interface ε in Eq. (14) for smearing out the viscosity is set to $1.5\Delta y$. A constant time step $\Delta t = 0.02H/c_{wave}$ is used for all cases. A no-slip wall boundary condition is applied to the left, right, and bottom boundaries and a slip wall boundary condition is applied at the top boundary. For level set function a linear extrapolation is used to set the boundary condition. The effects of left wall is considered to be negligible after $6H/c_{wave}$ time unit and then the normalized time is set to $T = 0$. Fig. 3 shows the solitary wave profiles at different times from $T = 0$ including its run-up on the right wall for case $A_0 = 0.4H$.

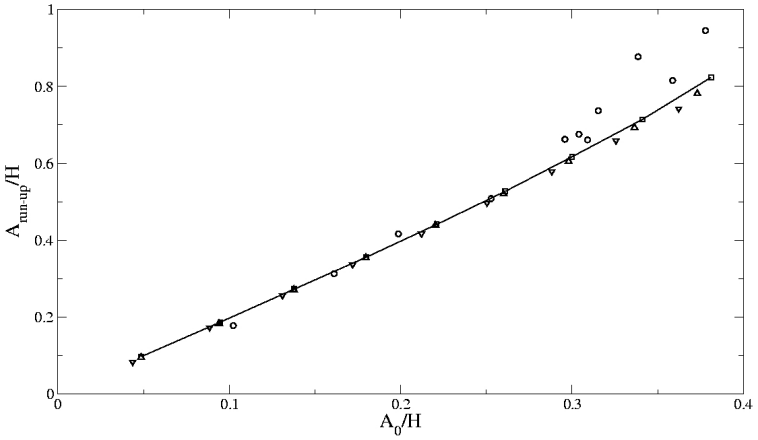

Figure 4. Run-up height as a function of incident amplitude for a solitary wave. ◯: Experimental data;[6] △: Finite volume simulation;[39] ▽: Finite element simulation;[24] □: Present simulation.

The computational results for a series of initial profile height A_0 are given in Fig. 4, which shows the run-up height A_{run-up} as a function of the incident amplitude A_c. The experimental data in Ref. 6 and a finite volume simulation[39] and a finite element simulation[24] are also given for comparison purpose. Good agreement with the experimental data until around $A_c/H = 0.3$ is observed. After $A_c/H > 0.3$, our calculations under-predict the run-up height. The main reason is that we start the calculation with a still Boussinesq profile in hydrostatic balance and zero velocity field. This approximation works well for small amplitude solitary waves, but not for large amplitude ones. Nevertheless, our results agree very well with other numerical results [39,24] that used the same Boussinesq profile for initial interface profile, although both of them used slightly finer grids (24000 cells in Ref. 39 and 23600 elements in Ref. 24) than the one used here.

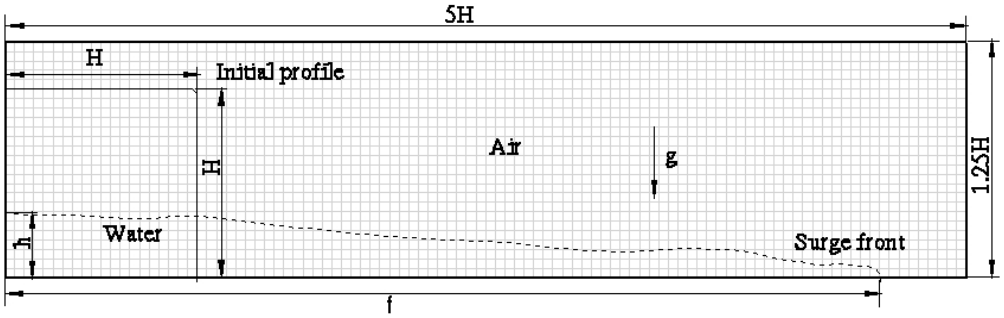

Figure 5. Sketch of computational setup and grid for a 2D dam-break problem.

IV.A.2. 2D Dam-break Problem

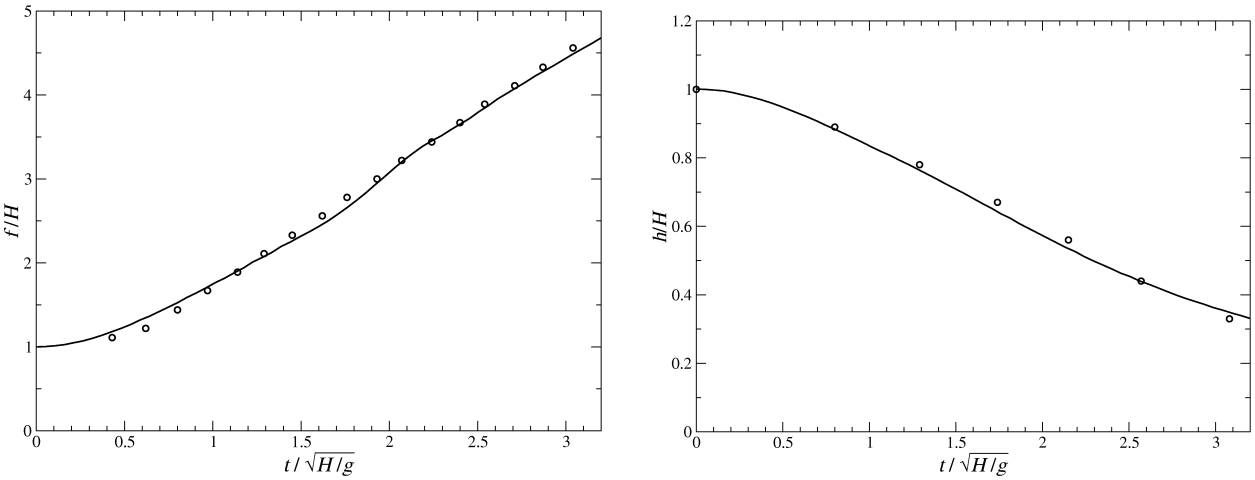

(a) (b)

Figure 6. 2D dam-break problem. (a) Surge front position at different times; (b) Remaining water column height at different times. ◯: Experimental data;[27] —: Present simulation.

Dam-break problem has been extensively studied by many authors. Here, the experimental study of the falling and spreading of a square water column of length $H = 2.25$ inch on a right horizontal plate by Ref. 27 is used for validation purpose. Fig. 5 shows the computational setup and grid. The domain size is $5H \times 1.25H$, which is the same as the one used in Ref. 21. The water column is initially blocked at rest on the left side of the enclosed box. At $t = 0$ the blocking is released and the water column starts to fall and spread out. The falling rate and spreading speed are measured by the remaining water column height h and the position of the surge front f. We use a uniform grid 100×25 and the time in the computation is normalized by $\sqrt{H/g}$. A no-slip wall boundary condition is applied to the all boundaries.

The comparison of numerical results and experimental data is shown in Fig. 6. Fig. 6 (a) and (b) give the surge front position and remaining water column height at different times, respectively. Both of them show good agreement between the experimental data and the present calculation.

IV.A.3. A 3D Rising Spherical Cap bubble in a Quiescent Liquid

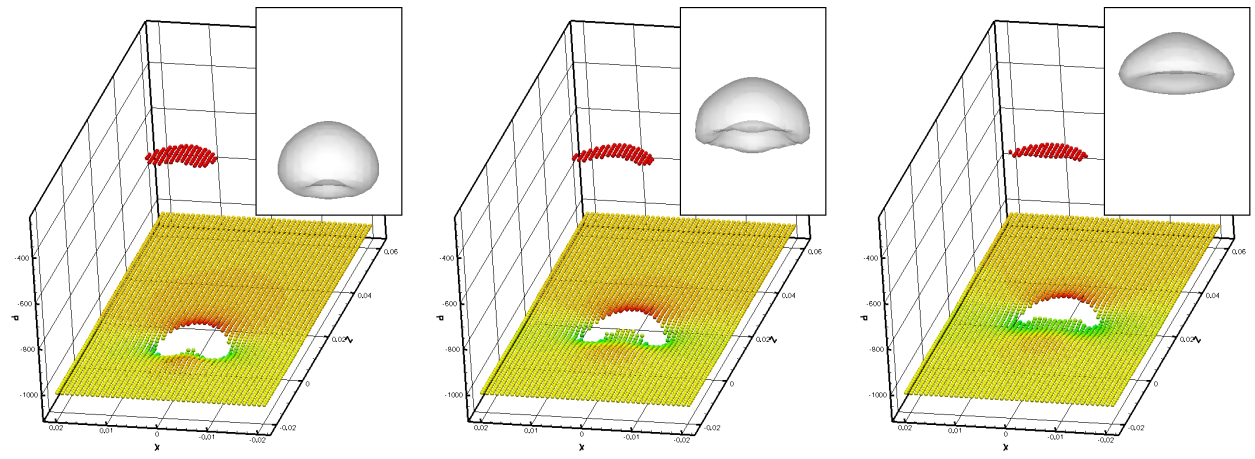

(a) $t = 0.03s$ (b) $t = 0.06s$ (c) $t = 0.09s$

Figure 7. A 3D rising spherical bubble in a quiescent liquid.

The spherical cap bubbles rising in a quiescent liquid were studied experimentally in Ref. 14. One of the cases we consider here has the following parameters: $\rho_L = 0.8755$ g cm^{-3}, $\rho_G = 0.001$ g cm^{-3}, $\mu_L = 1.18$ P, $\mu_G = 0.01$ P, and the surface tension coefficient $\sigma = 32.2$ dyn cm^{-1}. The volume of the bubble is 0.94 cm^{-3} and the corresponding effective radius is 0.608 cm.

The computational domain for this case is 4cm $\times$ 4cm $\times$ 8cm and grid size is $40\times40\times80$. Slip-wall boundary condition is applied to all boundaries. The dynamic pressure ($p-\rho g_z z$) profiles across the $x-z$ center plane of the bubble, with its shape evolution on the right top corner, for several instances are shown in Fig. 7. The sharp jump of pressure due to gravity and surface tension is evident. The steady rising speed from our computation is 21.0 cm s^{-1}, which is very close to that in the experiment 21.5 cm s^{-1}, although we use a very coarse grid here.

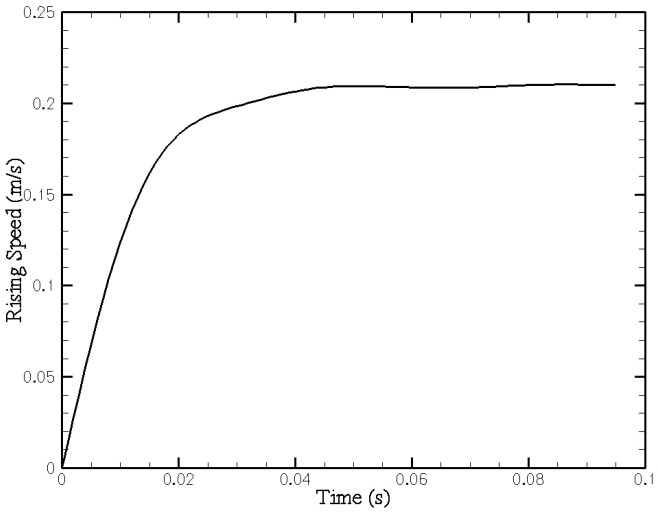

Figure 8. Rising speed of a 3D spherical bubble in a quiescent liquid.

IV.B. Spilling Breaking Waves Generated by a Submerged Hydrofoil

IV.B.1. 2D Non-breaking Waves

Here we first show a two-dimensional simulation of the non-breaking wave by a submerged NACA0012 hydrofoil. The computational setup is shown in Fig. 9. The Reynolds number based on the uniform inflow velocity U and the hydrofoil chord length L is $Re = \rho UL/\mu = 1.624 \times 10^5$, which is the same as that in the experiment.[12] The Froude number $Fr = U/\sqrt{gL} = 0.5672$. The hydrofoil has a constant positive 5° attack angle and a constant depth of submergence at the mid-chord position $d_s = 0.951$. The computational domain is $3L \times 19L$ with $6L$ ahead of the leading edge and $12L$ behind the trailing edge. A non-uniform Cartesian grid of 448×1024 is generated for this calculation with the smallest cell of size $0.001L$ near the leading and trailing edges. And a constant timestep of $\Delta t = 0.00025L/U$ is used.

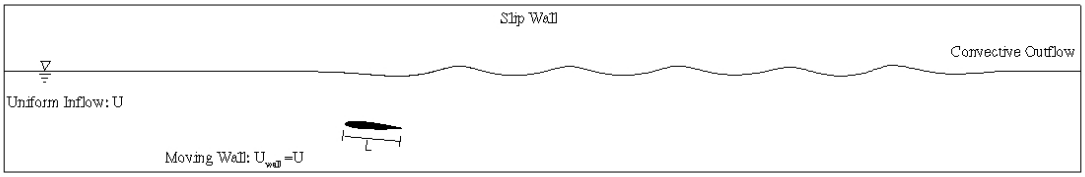

Figure 9. Computational domain for a submerged hydrofoil in a uniform flow.

The comparison of wave profiles from the experiment and the present simulation is given in Fig. 10. A fairly good agreement is observed. An instantaneous snapshot of the vortices shed from the hydrofoil is presented in Fig. 11 and the corresponding close-up around the hydrofoil is given in Fig. 12. At this depth of submergence, the free-surface profile is pretty steady. The shear layer from the separated boundary layer on the top of the hydrofoil becomes unstable very soon; a series of shed vortices roll over the foil surface until reaching the trailing edge and then interact with the detached boundary layer on the bottom of the foil. The vortex shedding pattern behind the hydrofoil is very similar to the $Re = 3 \times 10^4$ case by Chen and Chwang.[8] However, a feature missed in their results is the surface vorticity distribution as they solved only the liquid phase.

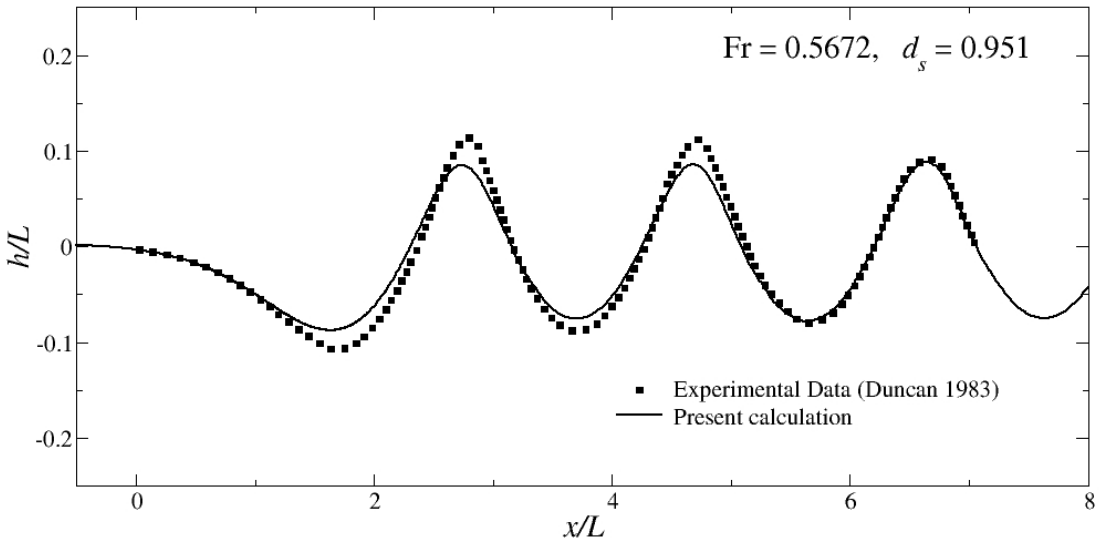

Figure 10. The profile of a steady wave generated by a submerged hydrofoil.

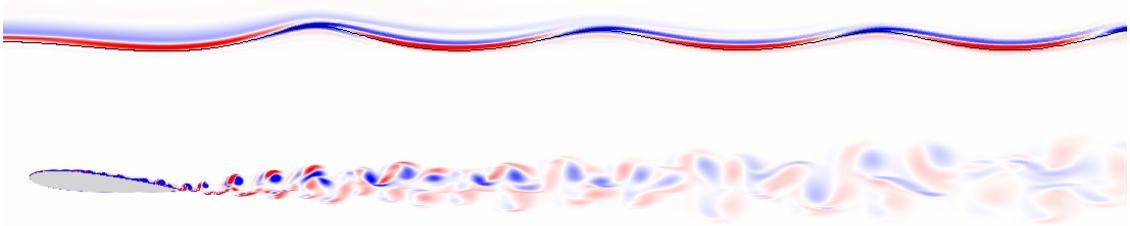

Figure 11. Instantaneous vorticity contours. Black line identifies the free surface.

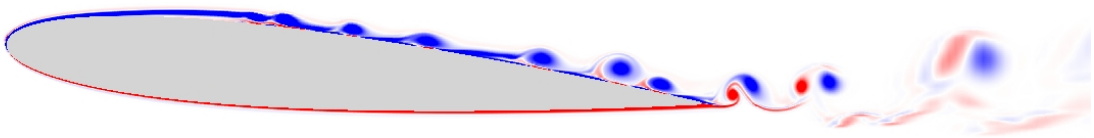

Figure 12. A close-up of the vorticity distribution near the hydrofoil.

IV.B.2. 3D Spilling Breakers

For the 3D case, we choose the one with a depth of submergence $d_s = 0.783$ in Duncan's experiment.[12] The Reynolds number and the Froude number are the same as those of the 2D case above. The same domain and grid in the $x - z$ plane are used. For the current study, a very limited domain size of half chord length in the spanwise direction and 32 uniform grid points are chosen, which gives a grid of 14.7 million points.

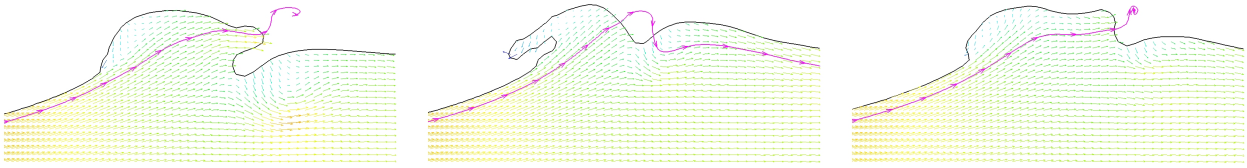

(a) (b) (c)

Figure 13. Instantaneous velocity vectors, only the water phase shown. Colored by the streamwise velocity.

Instantaneous snapshots of the velocity vectors in one $x-z$ plane at three different instances are given in Fig. 13. In the figures, only the vectors in the water phase are plotted. Both Fig. 13(a) and (c) show a rolling eddy riding on the forward face of the wave, which is very similar to what described in Ref. 12. At this depth of submergence, the spilling breakers are no longer steady or quasi-steady and they are intermitted by small plunging breakers, as shown in Fig. 13(b). The air entrainment process is captured, although the air/water mixture cannot be resolved with the current grid.

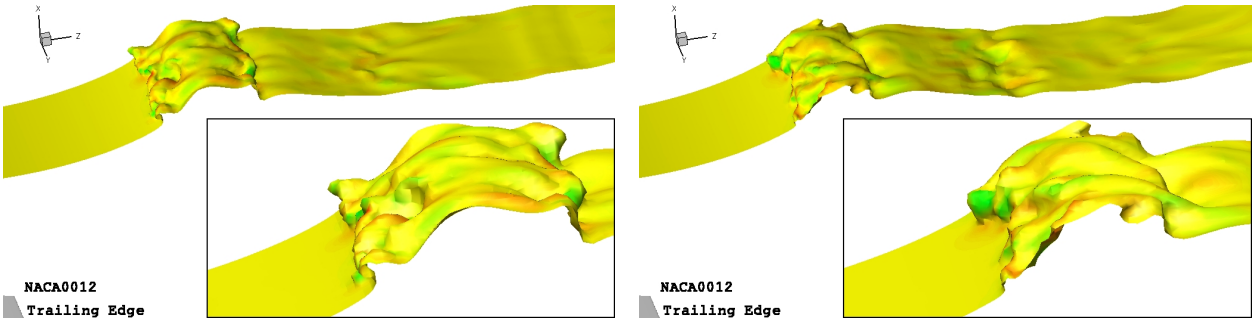

(a) (b)

Figure 14. Instantaneous free surface profiles. Colored by the streamwise vorticity.

Fig. 14 shows the instantaneous free surface profiles at two different times. The spilling and small plunging breakers are intermittent. They also interweave in the spanwise direction, which is indicated by the direction and magnitude of the streamwise vorticity used to color the free surface.

The vortical structures defined by the Q criterion[15] above and beneath the free surface and around the foil are displayed in Fig. 15. The neat organized vortices rolling over the foil surface shown in the 2D simulation no longer exist. For this case, numerous small structures are generated at the foil surface and transported downstream. In the water phase, many large, organized vortical structures are produced at the breaking points and then dissipated in the turbulent wake under the free surface. Interestingly, more vortical structures are generated in the air phase and they interacted with the free surface as they move downstream.

IV.C. Plunging Breaking Waves behind a Surface-mounted Bump

IV.C.1. 2D Impulsive Plunging Breaking Waves

The second case is the impulsive plunging breaking waves behind a surface-mounted bump. The computational domain, as shown in Fig. 16, is $2L \times 24L$ with $2L$ the bump length. A 2D simulation has been performed at $Re = 1,000$ and $Fr = 0.317$ based on the bulk inflow velocity and half bump length. The grid is 512×1024. Fig. 17 gives the instantaneous breaking wave profiles and vorticity contours at several instances. In the Figure, the overturning jet plunges onto the free surface and a rebounding jet splashes up and produces a second plunging jet, which splashes up again. The results presented here are very similar to the experimental results by Ghosh ($Re = 1.55 \times 10^5$)[13] and what is shown in[16] ($Re = 1 \times 10^4$). A shear layer separation from the bump is evident as a sudden-start initial condition is used here.

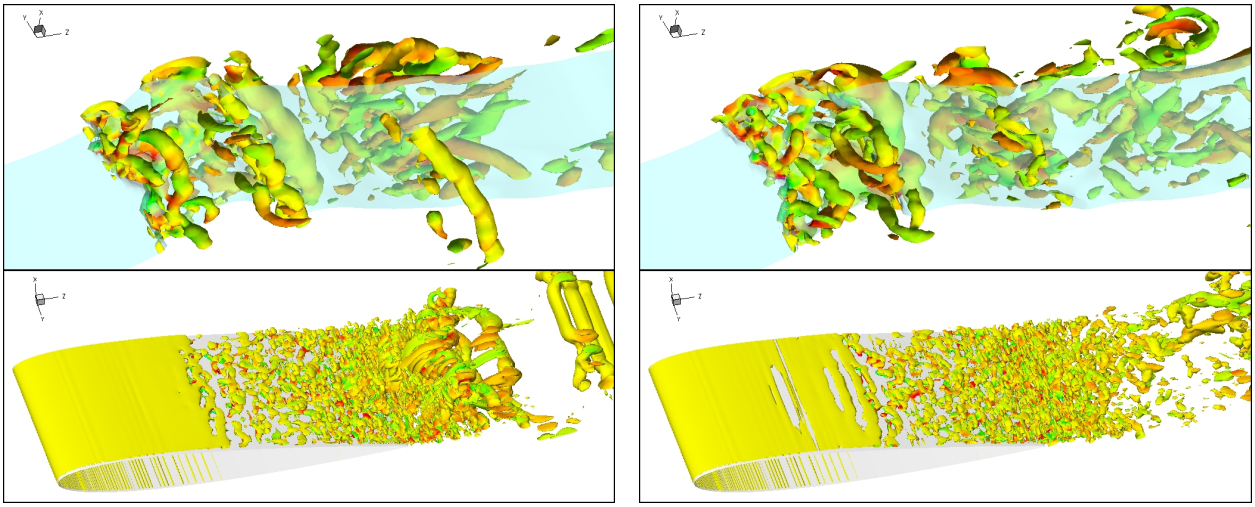

(a) (b)

Figure 15. Vortical structures. Colored by the streamwise vorticity.

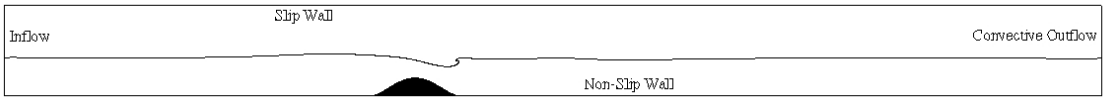

Figure 16. Computational domain for free-surface flow over a surface-mounted bump.

IV.C.2. 3D Impulsive Plunging Breaking Waves

The LES of the impulsive plunging breaking waves behind the bump is run at a higher Reynolds number $Re = 2 \times 10^5$ and coarser grid 256×512 in the $x - z$ plane. The spanwise size is $0.4L$ and 32 uniform grid points are used. When the plunging jet hits the water surface, violent splashes give rise to strong water-air interaction. The instantaneous free surface profiles and vortical structured are presented in Fig. 18 and Fig. 19, respectively.

V. Conclusions

In this paper, a sharp interface method has been developed for the large-eddy simulation of breaking waves generated by immersed bodies. The mathematical model is discussed and the numerical method has been validated using several test cases: 2D solitary wave propagation, 2D dam-break problem, and 3D rising bubble. Also, 2D results with immersed bodies, the non-breaking waves generated by a submerged hydrofoil, and impulsive plunging breaking waves behind a surface-mounted bump have been presented and good agreement with the experimental results has been obtained. Then the 3D LES of spilling breaking waves generated by the hydrofoil and plunging breaking wave behind the bump have been carried out and discussed.

The results shown in this paper demonstrate the great promise of current embedded-boundary/level-set approach in the detailed simulations of breaking waves. Nevertheless, the velocity in the normal direction of the immersed boundary is assumed to be a linear distribution in the embedded boundary method used

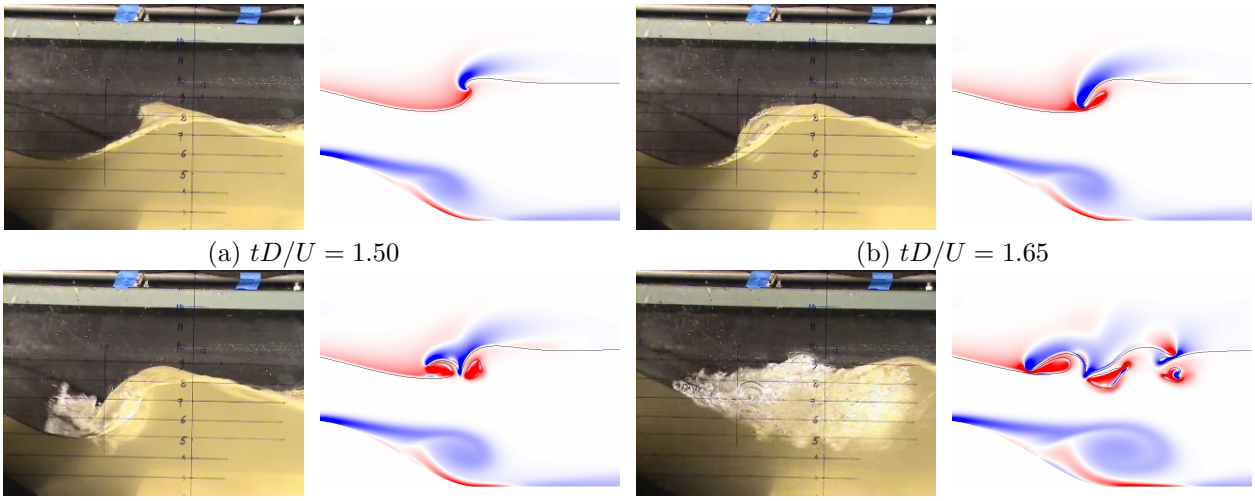

(a) $tD/U = 1.50$ (b) $tD/U = 1.65$

(c) $tD/U = 1.80$ (d) $tD/U = 2.40$

Figure 17. Instantaneous wave profiles (and vorticity contours from simulation). Left: experiment; Right: simulation.

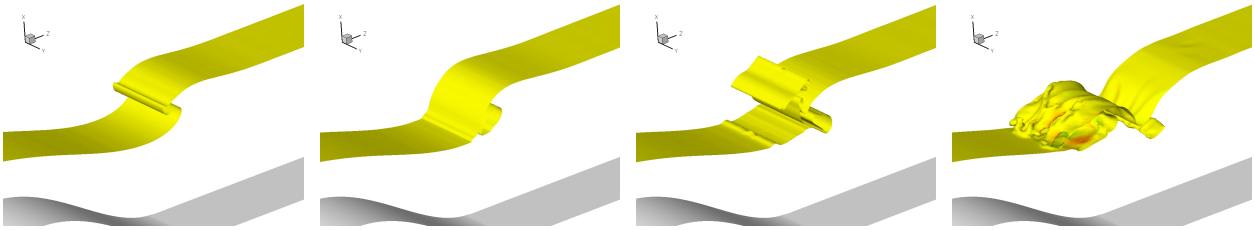

(a) (b) (c) (d)

Figure 18. Instantaneous free surface profiles. Colored by the streamwise vorticity.

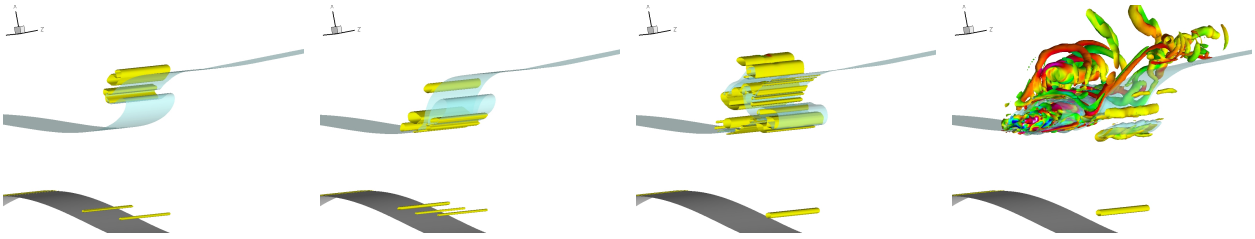

(a) (b) (c) (d)

Figure 19. Vortical structures. Colored by the streamwise vorticity.

here. For LES on coarse grids we need develop techniques to consider the non-linear distribution of velocity in the turbulent boundary layer. Also, a mixture model in the breaking region is necessary to fully take the water-air interaction into account. To further validate our code and as a necessary step towards the LES of ship flows, the steady/quasi-steady spilling breakers generated by a NACA0012 hydrofoil and the plunging breakers by a surface-mounted bump will be investigated. In Ghosh's experiment,[13] a periodic plunging breaking wave case with a very low Froude number has been investigated and plentiful interesting phenomena have been discovered. Basically, as the inflow velocity increases, the flow behind the bump goes through several different stages: smooth, two-dimensional non-breaking waves; non-smooth, three-dimensional non-breaking waves with spanwise instability; three-dimensional spilling breaking waves; and finally periodic three-dimensional plunging breaking waves. We will perform the simulation of this periodic plunging breaking wave case and compare with the 3D stereo PIV experimental results as our future work.

Acknowledgments

This research is sponsored by the Office of Naval Research under Grant N00014-01-1-0073, under the administration of Dr. Patrick Purtell.

References

[1]E. Balaras, Modeling complex boundaries using an external force field on fixed Cartesian grids in large-eddy simulations, Comput. Fluids, 33 (2004) 375–404.

[2]E. Balaras, J. Yang, Non-boundary conforming methods for large-eddy simulations of biological flows, ASME J. Fluids Eng., 127 (2005) 851-857.

[3]S. Balay, W.D. Gropp, L.C. McInnes, B.F. Smith, Efficient management of parallelism in object oriented numerical software libraries, in Modern Software Tools in Scientific Computing, Edited by E. Arge, A.M. Bruaset, H.P. Langtangen, Birkhäuser Press, (1997) 163–202.

[4]R.M. Beam, R.F. Warming, An implicit finite-difference algorithm for hyperbolic systems in conservation-law form, J. Comput. Phys., 22 (1976) 87–110.

[5]P.M. Carrica, R.V. Wilson, F. Stern, Unsteady RANS simulation of the ship forward speed diffraction problem, Comput. Fluids, 35 (2006) 545–570.

[6]R.K.-C. Chan, R.L. Street, A computer study of finite-amplitude water waves, J. Comput. Phys., 6 (1970) 68-94.

[7]Y.C. Chang, T.Y. Hou, B. Merriman, et al., A level set formulation of Eulerian interface capturing methods for incompressible fluid flows, J. Comput. Phys., 124 (1996) 449–464.

[8]T. Chen, A.T. Chwang, Trailing vortices in a free-surface flow, Phys. Fluids, 14 (2002) 827–838.

[9]H. Choi, P. Moin, Effects of the Computational Time Step on Numerical Solutions of Turbulent Flow, J. Comput. Phys., 113 (1994) 1–4.

[10]E.D. Christensen, R. Deigaard, Large eddy simulation of breaking waves, Coastal Engineering, 42 (2001) 53–86.

[11]E.D. Christensen, Large eddy simulation of spilling and plunging breakers, Coastal Engineering, 53 (2006) 463–485.

[12]J.H. Duncan, The breaking and non-breaking wave resistance of a two-dimensional hydrofoil, J. Fluid Mech., 126 (1983) 507–520.

[13]S. Ghosh, Experimental study of plunging breaking waves, PhD thesis, IIHR, University of Iowa, 2006, in progress.

[14]J.G. Hnat, J.D. Buckmaster, Spherical cap bubbles and skirt formation, Phys. Fluids, 19 (1976) 182-194.

[15]J.C.R. Hunt, A.A. Wray, P. Moin, Eddies, streams and convergence zones in turbulent flows, Center for Turbulence Research, Proceedings of the Summer Program, 1988, p. 193.

[16]A. Iafrati, A. Di Mascio, E.F. Campana, A level set technique applied to unsteady free surface flows, Inter. J. Numer. Methods Fluids, 35 (2001) 281–297.

[17]G.-S. Jiang, D. Peng, Weighted ENO schemes for Hamilton–Jacobi equations, SIAM J. Sci. Comput., 21 (2000) 2126-2143.

[18]G.-S. Jiang, C.-W. Shu, Efficient Implementation of Weighted ENO Schemes, J. Comput. Phys., 126 (1996) 202–228.

[19]M. Kang, R.P. Fedkiw, X.-D. Liu, A Boundary Condition Capturing Method for Multiphase Incompressible Flow, Journal of Scientific Computing, 15 (2000) 323–360

[20]J. Kim, D. Kim, H. Choi, An Immersed-Boundary Finite-Volume Method for Simulations of Flow in Complex Geometries, J. Comput. Phys., 171 (2001) 132–150.

[21]F.J. Kelecy, R.H. Pletcher, The development of a free surface capturing approach for multidimensional free surface flows in closed containers, J. Comput. Phys., 138 (1997) 939-980.

[22]E.V. Laitone, The second approximation to cnoidal and solitary waves, J. Fluid Mech., 9 (1960) 430–444.

[23]B.P. Leonard, Stable and accurate convective modeling procedure based on quadratic upstream interpolation, Computer Methods in Applied Mechanics and Engineering, 19 (1979) 59–98.

[24]C.-L. Lin, H. Lee, T. Lee, L. Weber, A Level Set Characteristic Galerkin Finite Element Method for Free Surface Flows, Inter. J. Numer. Methods Fluids, 49 (2005), 521–547.

[25]X.D. Liu, R. Fedkiw and M. Kang, A boundary condition capturing method for Poissons equation on irregular domains, J. Comput. Phys., 154 (2000), p. 151–178.

[26]P. Lubin, S. Vincent, S. Abadie, J.P. Caltagirone, Three-dimensional Large Eddy Simulation of air entrainment under plunging breaking waves, Coastal Engineering, 53 (2006) 631–655.

[27]J.C. Martin, W.J. Moyce, An experimental study of the collapse of liquid columns on a rigid horizontal plate, Phil. Trans. Royal Soc. London Ser. A, 244 (1952) 312-324.

[28]N. Mattor, T.J. Williams, D.W. Hewett, Algorithm for solving tridiagonal matrix problems in parallel, Parallel Computing, 21 (1995) 1769–1782.

[29]C. Meneveau, C.S. Lund, W.H. Cabot, A Lagrangian dynamic subgrid-scale model of turbulence. J. Fluid Mech., 319 (1996) 353–385.

[30]D. Peng, B. Merriman, S. Osher, H. Zhao, M. Kang, A PDE-Based Fast Local Level Set Method, J. Comput. Phys., 155 (1999) 410–438.

[31]B. Ramaswamy, Numerical simulation of unsteady viscous free surface flow, J. Comput. Phys., 90 (1990) 396–430.

[32]C.-W. Shu, S. Osher, Efficient implementation of essentially non-oscillatory shock-capturing schemes, J. Comput. Phys., 77 (1988) 439–471.

[33]M. Sussman, P. Smereka, S. Osher, A Level Set Approach for Computing Solutions to Incompressible Two-Phase Flow, J. Comput. Phys., 114 (1994) 146–159.

[34]M. Sussman, K.M. Smith, M.Y. Hussaini, M. Ohta, R. Zhi-Wei, A sharp interface method for incompressible two-phase flows, J. Comput. Phys., In Press, (2006) doi:10.1016/j.jcp.2006.06.020.

[35]F. Tessicini, G. Iaccarino, M. Fatica, M. Wang, R. Verzicco, Wall modeling for large-eddy simulation using an immersed boundary method, Annual Research Briefs 2002, Center for Turbulent Research.

[36]Y. Watanabe, H. Saeki, R.J. Hosking, Three-dimensional vortex structures under breaking waves, J. Fluid Mech., 545 (2005) 291–328.

[37]R.V. Wilson, P.M. Carrica, F. Stern, Unsteady RANS method for ship motions with application to roll for a surface combatant, Comput. Fluids, 35 (2006) 501–524.

[38]J. Yang, E. Balaras, An embedded-boundary formulation for large-eddy simulation of turbulent flows interacting with moving boundaries, J. Comput. Phys., 215 (2006) 12–40.

[39]W. Yue, C.-L. Lin, V.C. Patel, Numerical simulation of unsteady multidimensional free surface motions by level set method , Int. J. Numer. Meth. Fluids, 42 (2003) 853-884.